communications earth & environment

Article

https://doi.org/10.1038/s43247-024-01258-1

Marine heatwaves and cold spells in the Brazil Overshoot show distinct sea surface temperature patterns depending on the forcing

Check for updates

Hao Liu [1,2,3,4] ✉, Xunwei Nie [2,3,4], Junqiang Shi [1] & Zexun Wei [2,3,4] ✉

The Brazil Current Overshoot regions feature the strongest sea surface temperature variations over the global ocean but forecast skill for these extreme variations is limited. Here we investigate the drivers of marine heatwaves and cold spells in this region and find that ocean flows and sea surface heat fluxes are the primary drivers. We also find that sea surface temperature extremes driven by air-sea heat fluxes produce consistent changes in sea surface temperature and related atmospheric variables over a wide horizontal area, whereas ocean flow-driven sea surface temperature extremes exhibit low consistency in air variables and limited consistency in the spatial extent of sea variables across most sea surface temperature extreme events. These differing air-sea characteristics associated with extremes driven by different drivers offer potential avenues for improving prediction skills and advancing the understanding of three-dimensional air-sea impacts associated with extreme events.

The collision of the two opposite western boundary currents in the western South Atlantic Ocean has formed the Brazil-Malvinas confluence (BMC, Fig. 1a). The southward western boundary current is called the Brazil Current (BC). When it encounters the northward Malvinas Current (MC) near 38°S, this current separates away from the eastern coast of the South American continent, continuing south and retroflecting northward at 45°S[1]. This V-word-shaped flow in the BMC is called the Brazil Current Overshoot (BCO, Fig.1b). The BCO favors energy transfer from the mean current to mesoscale flows[2], producing strong meanders, eddies, and filaments. It is one of the most energetic mesoscale regions over the global ocean[3]. The strong ocean front and mesoscale eddies over the BMC and the BCO regions favor the exchanges of salt and heat and account for 50% of the total subduction rate in the South Atlantic Ocean and approximately 50% of the cross-Antarctic Circumpolar Current poleward heat flux over the global ocean[4]. The mixture of different types of water[5] promotes and sustains high phytoplankton diversity[6–8].

The BCO (also denoted as Brazil Current extensions in the literature) is a hot spot of global warming[9,10]. The enhanced eddy (see definition in the Methods section) generation over the eddy-rich region has led to enhanced ocean warming[3] over recent decades through the poleward shift of western boundary currents. Furthermore, both anticyclonic and cyclonic eddies that originated and decoupled from the BC could bring warmer toward the pole, and they warm air-sea systems over the BCO[11]. Thus, the increased number of eddies can warm the sea surface.

Marine ecosystems are highly vulnerable to ocean warming. For example, ocean subsurface warming can lead to the tropicalization of demersal megafauna within the South Atlantic subtropical gyre[12]. Marine heatwaves (MHWs), denoted as prolonged periods of anomalously high sea surface temperature (SST) on the weather time scale[13], can also cause devastating impacts on the marine environment in the southwestern South Atlantic Ocean. The most intense MHW occurred during the austral summer of 2017, resulting in tons of dead fish and algae blooms along the coast of Montevideo[14]. Similarly, the MHW in 2013/14 was associated with adjacent droughts in Brazil, leading to a tripled number of fatalities due to a fever outbreak[15]. Although the characteristics of MHWs have been studied extensively in the vicinity of the coastal ocean of the southwestern South Atlantic, their characteristics in the eddy-rich BCO remain poorly understood. The opposite of an MHW is a cold spell (MCS), which occupies the cold end of the temperature range[16]. The characteristics of cold spells are also less investigated.

[1]Institute of Oceanographic Instrumentation, Qilu University of Technology (Shandong Academy of Science), Qingdao, China. [2]Laboratory for Regional Oceanography and Numerical Modeling, Laoshan Laboratory, Qingdao, China. [3]First Institute of Oceanography, and Key Laboratory of Marine Science and Numerical Modeling, Ministry of Natural Resources, Qingdao, China. [4]Shandong Key Laboratory of Marine Science and Numerical Modeling, Qingdao, China.
✉e-mail: liuhao@qlu.edu.cn; weizx@fio.org.cn

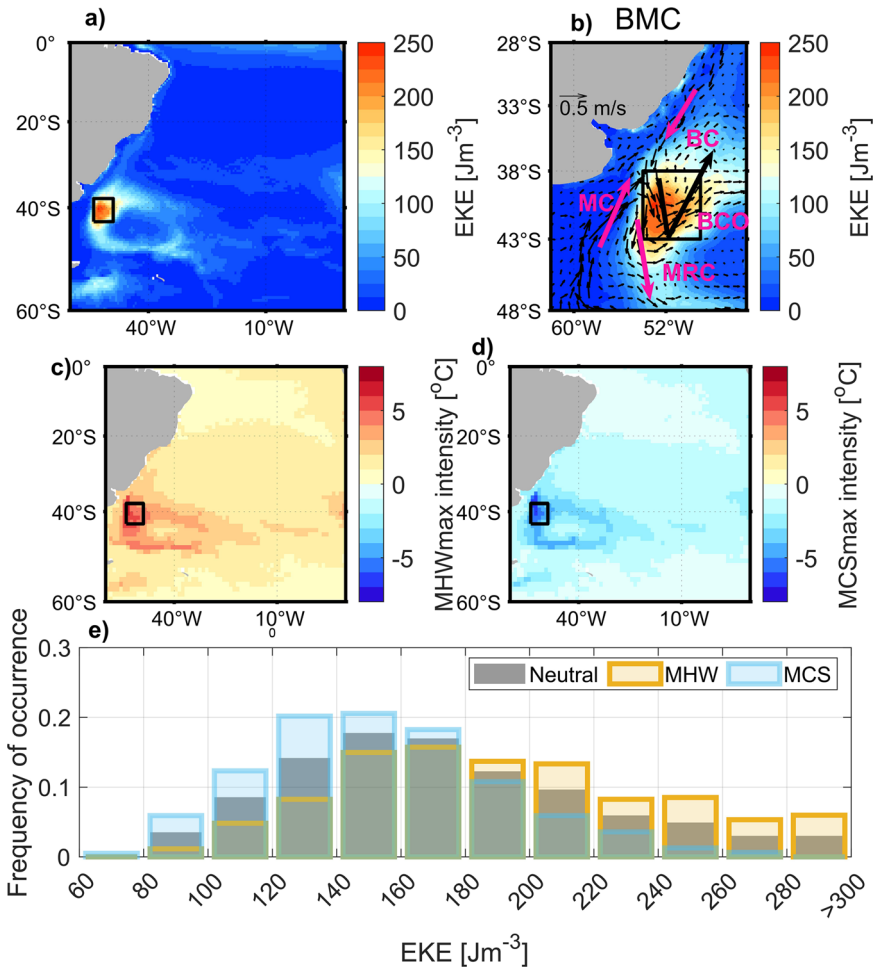

Fig. 1 | Relationship between EKE and the intensity of SST extreme events. a The spatial distribution of climatological mean EKE. **b** The spatial distribution of EKE and velocities (thin black arrows) over the BMC. BC denotes the Brazil Current, MC denotes the Malvinas Current, MRC denotes the Malvinas Return Current and BCO denotes the Brazil Current Overshoot. The thick black arrow denotes the flow patterns of the BCO, and the magenta arrows denote the directions of other currents. **c** The spatial distribution of the maximum intensity of the MHWs. **d** Spatial distribution of the maximum intensity of the MCSs. **e** Probability distribution of MHWs (orange), MCSs (blue) and the neutral phase (SST anomalies lie between the 10th and 90th percentiles) against the strength of the EKE over the BCO (black box). All panels were calculated over the 1993-2020 period. The black boxes in a, b, c and d denote the BCO region with a high EKE and a large magnitude of extreme SST events.

Previous research has shown that MHWs driven by different local drivers, such as atmospheric and oceanic factors, have different spatial SST patterns. MHWs driven by air-sea heat fluxes show an extended area of positive SST anomalies[17], while MHWs driven by ocean currents exhibit deeper vertical extensions[18]. However, other than SST anomalies, the spatial states of different air-sea variables associated with MHWs remain generally less investigated yet important to both ecosystems and maritime activity. Therefore, further research is necessary to fully comprehend the complexities surrounding extreme SST events.

The Coupled Model Intercomparison Project 5 (CMIP5) models show the most disagreement over the BCO with observations and among themselves in past and future MHWs[19]. The BCO is associated with the lowest MHW forecast skill[20], which is possibly attributed to the lack of a dominant driver of climate modes responsible for MHW occurrence within this region[21]. By understanding the local drivers of extreme SST events and their associated changes in air-sea patterns, we will be able to better understand their potential predictability.

Here, we conduct a joint analysis of a set of well-established reanalysis data to investigate the local drivers of MHWs and MCSs over the BCO and explore their associated air-sea patterns. The main objective of this study is to establish a relationship between drivers of SST extremes and changes in their respective air-sea states and characteristics. Through this analysis, we aim to enhance our understanding of the unique features exhibited by MHWs and MCSs in eddy-rich regions. The Results section comprises an examination of the connection between eddy dynamics and the intensity of SST extremes. Additionally, we utilize a mixed layer temperature budget, as outlined in previous studies[22,23], to identify the local drivers of MHWs and MCSs. Furthermore, we present the air-sea states during heat flux-driven and advection-driven MHWs/MCSs. In the Discussion section, we provide a summary of our findings, discuss the implications of this study, and compare our results with previous analyses.

Results

Sea surface temperature extremes over the BCO

The South Atlantic exhibits maximum eddy kinetic energy (EKE) in the BCO region (Fig. 1a, b). This large EKE can be attributed to increased eddy generation/dissipation frequency[24] and/or the larger amplitude of eddies[25], which exceeds those found in most of the global ocean[26]. The unique characteristics of EKE observed over the BCO are a result of its consistent drain on energy from the time-mean flows[27].

The magnitude of SST anomalies associated with the maximum intensity of MHWs and MCSs is substantial (>±5 °C) over the BCO (Fig. 1c, d). This magnitude is higher than most of the recorded MHWs across the rest of the globe and has serious consequences for both human and natural systems[28]. The maximum intensity of MHWs (Fig. 1c) occurs in regions of enhanced eddies, in agreement with the theory of "warmer over eddy-rich regions"[3,10]. The maximum intensity of MCSs (Fig. 1d) also corresponds to areas of high eddy activity (compared in a spatial perspective), indicating the possible role of eddies (or their absence) in driving MCSs. MHWs are more prone to occur during high-EKE events (compared in a temporal perspective) over the BCO (Fig. 1e), with a peak occurrence in the 160–180 J m^{-3} EKE range. In contrast to MHWs, MCSs preferably occur over lower EKE in the BCO region, with a peak occurrence of 140–160 J m^{-3}.

Increased eddy activity is commonly linked to greater horizontal heat transport[29] and increased vertical heat exchange facilitated by eddy-induced Ekman pumping[30]. Figure 1 demonstrates that the relationship between eddy strength and sea surface warming/cooling also exists on a synoptic weather time scale, and an increased/attenuated EKE strengthens the

likelihood of the occurrence of MHWs/MCSs. It should be noted that while there is a strong connection between EKE strength and the occurrence of MHWs/MCSs, this does not imply a tight relation between coherent mesoscale eddies and SST extremes. Our statistical analysis reveals that the impact of coherent eddies on SST extremes is limited (see supplementary discussion 1 and Supplementary Fig. 1). This suggests that other contributing factors or forces may play an important role in driving the occurrence of SST extremes.

Local drivers of marine heatwaves and cold spells

To fully understand the relationship between EKE and extreme SST events across BCO regions, we calculate the mixed layer temperature budget[22,23] by taking into account the daily variations in mixed layer depth[17]. Our findings indicate that horizontal advection serves as the primary driver (see methods for details) of MHWs and MCSs over most of the South Atlantic Ocean, especially the BCO (Fig. 2a, b). These results are consistent with those reported by Marin et al.[22], who demonstrated that advection also plays a dominant role in the onset and decay of MHWs, albeit with a different model configuration. There are clear differences in dominant terms between MHW and MCS events over the 20 °S zonal band. Heat fluxes dominate during MHW events, while the advection term dominates during MCS events. It results from stronger heat fluxes and weaker advection terms during MHWs (supplementary discussion 2 and Supplementary Fig. 2).

The probability distribution of dominant drivers for MHWs (Fig. 2c) reveals that approximately 37% of MHWs in the BCO regions are attributed to horizontal advection, making it the primary driver of extreme SST anomalies in the area. The second most influential driver during MHWs is air-sea heat fluxes (accounting for 25% of the total MHW occurrence). On the other hand, the combined effects of vertical entrainment, mixed events (in which more than one term is in the dominance), and residual terms contribute to less than 40% of MHW occurrence.

In the BCO regions, during MCSs, the dominant factor is advection, which accounts for 35% of the occurrence of SST extreme events, while heat fluxes also play a prominent role, contributing to 33% of the total MCSs. Similar results were reported in the eddy-rich region within the South Pacific western boundary current systems[18], where heat fluxes contributed to over 30% of the MHW occurrence. This highlights that heat fluxes cannot be neglected in generating extreme SST events over advection-dominant regions with a high concentration of eddies. Moreover, heat flux-driven MHWs (HFlux-driven MHWs, see method for definition) in 2013/14 over the western South Atlantic Ocean were accompanied by severe drought in eastern South America[15]. Thus, the characteristics of atmospheric and ocean processes during MHWs and MCSs warrant further investigation.

During both MHWs and MCSs, the latent heat flux is the dominant component of net heat fluxes (Fig. 2d). In fact, the latent heat flux contributes to more than 60% of the net heat fluxes, making it an important factor in these extreme events. The second dominant term is solar radiation, which also plays a role in contributing to net heat fluxes. Recent studies in the eddy-rich region of the Tasman Sea have found similar results, whereby the latent heat flux is the dominant driver of heat fluxes in this region[17,18]. This implies that the latent heat flux might be a common driver of HFlux-driven MHWs in the eddy-rich western boundary current extension.

To further identify the key components in the horizontal advection terms (Fig. 2e), the ADV-driven MHWs and MCSs are divided into two terms. Mesoscale flows are the main contributors to the advection in MHWs. This feature is consistent with the strong connection between EKE and SST extreme events, as demonstrated in Fig. 1. During MCSs, both mean flows (Methods section) and mesoscale flows are important to heat advection.

Air and sea patterns during SST extreme events

SST extreme events caused by different drivers are associated with distinct air and sea states during their onset phase (as defined in the methods section, Figs 3 and 4). In HFlux-driven MHWs/MCSs, positive and negative SST anomalies exhibit a larger spatial extent than those in advection-driven MHWs/MCSs (Fig. 3a–d). Similar observations have been reported in the Tasman Sea[17,31] and on the southwestern flanks (on the northern side of the BCO) of the South Atlantic[15]. In contrast, SST anomalies in ADV-driven MHWs are typically confined to the BCO region.

Positive sea level pressure (SLP), latent heat flux, 200 hPa geopotential height and negative cloud cover/wind stress are found over an extended area during Hflux-driven MHWs (Fig. 3e, i, m, q, u). Conversely, these same variables are typically insignificant at a 95% confidence level over the southwestern South Atlantic subtropical gyre during ADV-driven MWHs (Fig. 3f, j, n, r, v). Positive SLP anomalies in Hflux-driven MHWs are associated with low-level air divergence, which leads to a decrease in cloud cover due to suppressed convection. Additionally, weakened wind stress leads to a decrease in evaporation cooling, resulting in positive latent heat

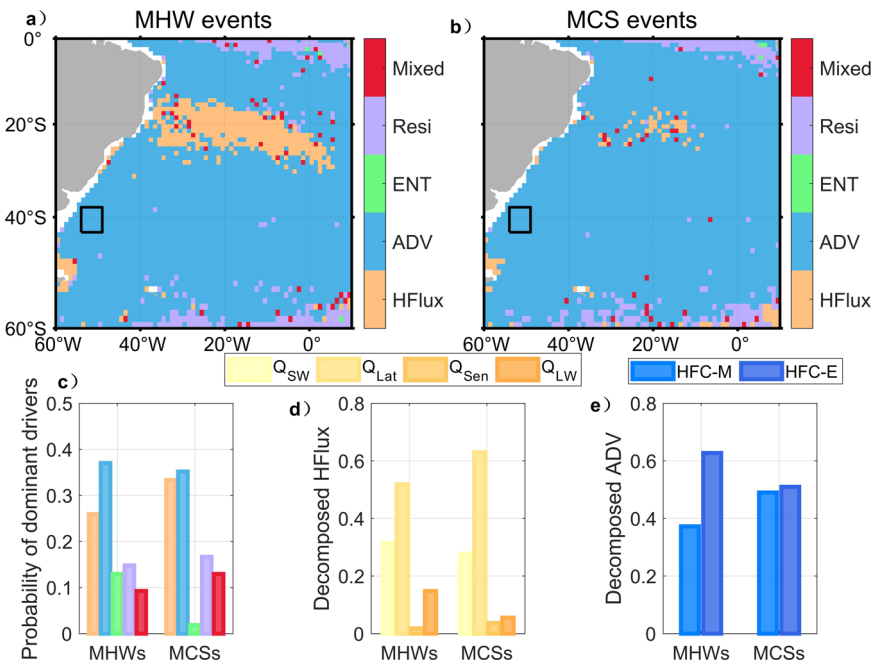

Fig. 2 | The local drivers of MHWs and MCSs over the western South Atlantic Ocean. a The main drivers of MHWs at each grid point over the 1993-2020 period. **b** The same as in **a**, but for the MCSs. The black boxes in a and b denote the BCO region. **c** The probability of the dominant drivers of MHWs and MCSs over the BCO. **d** The dominant heat flux during MHWs and MCSs (decomposed into solar radiation, latent heat flux, sensible heat flux, and longwave radiation). **e** The dominant advection term during MHWs and MCSs (decomposed into advection by mean flows and advection by mesoscale flows). Blanks in (**a**) denote grid points with a depth of less than 100 m. The orange bar in (**c**) denotes the heat flux term, the light blue bar denotes the horizontal advection term, the green bar denotes the entrainment, the purple bar denotes the residual term, and the red bar denotes that multiple terms are dominant simultaneously.

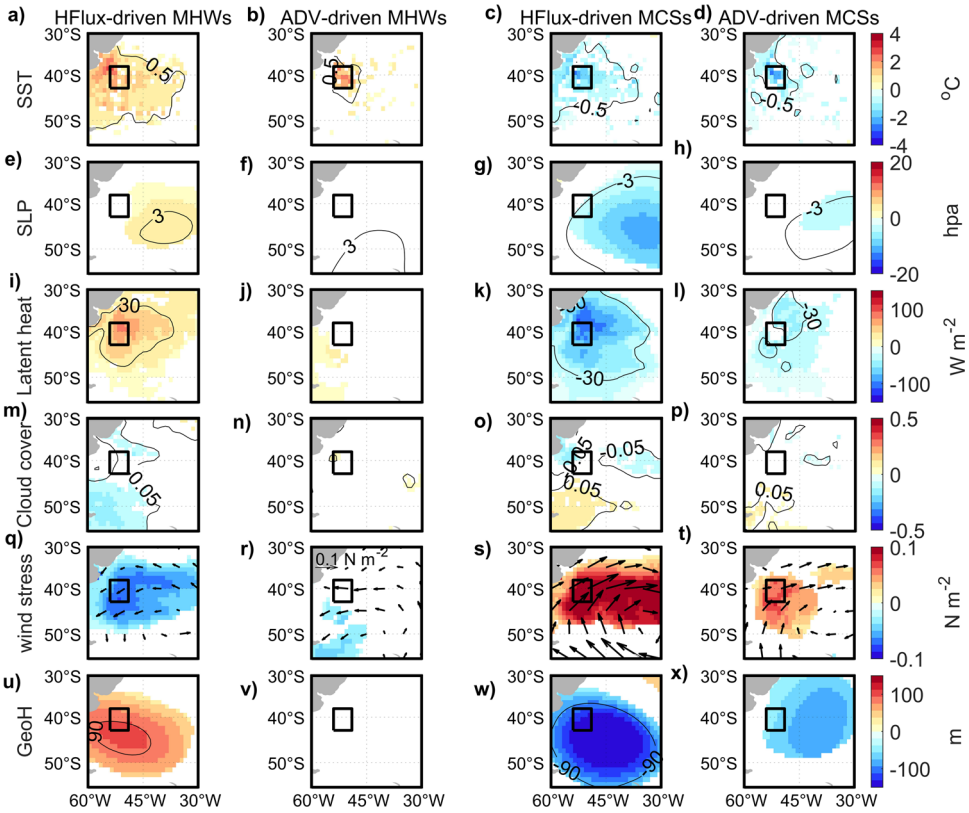

Fig. 3 | Atmospheric states during the onset phase (from the start time to peak time) of different types of SST extreme events. Composites of anomalies. **a**–**d** SST. **e**–**h** SLP. **i**–**l** Latent heat flux. **m**–**p** Cloud cover. **q**–**t** Wind stress. **u**–**x** Geopotential height at 200 hpa. **a**, **e**, **i**, **m**, **q**, and **u** denote cases during HFlux-driven MHW events. **b**, **f**, **j**, **n**, **r**, **v** denote cases during ADV-driven MHW events. **c**, **g**, **k**, **o**, **s**, **w** denote cases during HFlux-driven MCS events. **d**, **h**, **l**, **p**, **t**, **x** denote cases during ADV-driven MCS events. The color shadings denote regions with anomalies significant at the 95% confidence level (see methods for details). The vectors in subpanels (**q**-**t**) denote wind stress (N m^{-2}). The black contours denote the isolines of each variable without considering the 95% confidence level. The black boxes denote the BCO regions.

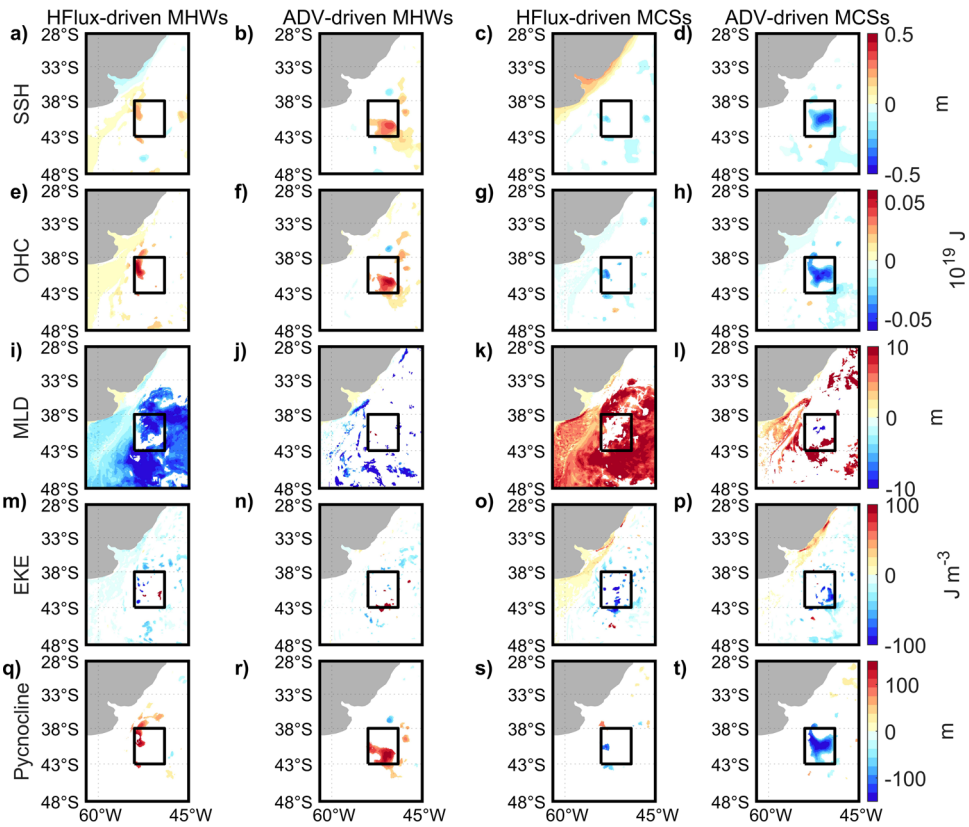

Fig. 4 | Ocean states during the onset phase of different types of SST extreme events. Composites of anomalies. **a**–**d** SSH. **e**–**h** 0-900 m OHC. **i**–**l** MLD. **m**–**p** EKE. **q**–**t** pycnocline depth (defined as the depth of 27kgm^{-3} isopycnal). **a**, **e**, **i**, **m**, and **q** denote cases during HFlux-driven MHW events. **b**, **f**, **j**, **n** and **r** denote cases during ADV-driven MHW events. **c**, **g**, **k**, **o** and **s** denote cases during HFlux-driven MHW events. **d**, **h**, **l**, **p** and **t** denote cases during ADV-driven MCS events. The color shadings denote regions with anomalies significant at the 95% confidence level. The black boxes denote the BCO regions.

fluxes and a warm ocean[15,32]. Composites of geopotential height anomalies in the upper troposphere (200 hPa) during Hflux-driven MHWs coincide with anomalous anticyclonic circulation and positive SLP anomalies, which suggests that blocking events control local weather systems[15]. The blocking could be part of a stationary Rossby wave train associated with the Madden–Julian Oscillation (MJO) originating in the Indian Ocean[15] or associated with a global wavenumber-4[33]/asymmetric Southern Annular Mode wavenumber-3 atmospheric wave[17]. SLP anomalies are typically larger over the southeastern side of the BCO due to their eastward propagation during the onset phase, which is in line with the paradigm of stationary waves leading to changes in SST[33].

Large magnitudes of SLP, latent heat flux, cloud cover, wind stress, and 200 hPa geopotential height occur during Hflux-driven MCSs (Fig. 3g, k, o, s, w), whereas ADV-driven MCSs exhibit a smaller magnitude or insignificant distribution of these variables (Fig. 3h, l, p, t, x). Negative SLP anomalies, negative 200 hPa geopotential height, and anomalous cyclonic circulation (Fig. 3s) suggest enhanced convection, leading to an increase in cloud cover (Fig. 3o). Similarly, an increase in wind stress leads to enhanced surface cooling (Fig. 3k).

Compared to atmospheric variables, most ocean variables exhibit significant changes over smaller spatial extent in the BCO (Fig. 4). The composite of sea surface height (SSH, which can be used as proxy for the position of BC[34]), 0-900 m ocean heat content (OHC, 900 m is defined as the lower limit because the BC is generally above 900 m in GLORYS12V1 data[34]), and sea surface EKE anomalies (Fig. 4a, c, e, g, m, o) show insignificant values over most of the BCO and its surrounding area in HFlux-driven MHWs and MSCs. In contrast, in ADV-driven MHWs, we observe significantly positive SSH and OHC on the southern flanks of the BCO, with negative values occurring on its eastern side in MCSs (Fig. 4b, d, f, h). Changes in SSH and OHC are associated with changes in SST, which can be attributed to changes in horizontal flows. The BC and its associated eddies transport warm waters to the BCO[11,35], resulting in pronounced effects on the OHC during ADV-driven MHWs/MCSs. These results suggest that extreme sea surface events are deeply expressed in the subsurface layer of the BCO due to oceanic circulation. Similar expressions are also reported in the East Australian Current system, where the deepest MHWs are associated with changes in oceanic circulation[18]. In addition, vertical processes also play a significant role in modulating SST anomalies during ADV-driven MHWs/MCSs. In the southern hemisphere, positive wind stress curl (shown as anticlockwise vectors in Fig. 3r) induces a deepening of the pycnocline depth due to Ekman pumping (Fig. 4r), which, in turn, can lead to a warming of the sea surface during adv-MHW events. Conversely, negative wind stress curl associated with Ekman suction (illustrated by clockwise vectors in Fig. 3t) causes uplift of the pycnocline depth (Fig. 4t), resulting in the upwelling of subsurface water and the subsequent cooling of the sea surface. Conversely, consistent changes in pycnocline depths are not observed in HFlux-driven MHWs and MSCs (Fig. 4q, s).

The composite of mixed layer depth (MLD) anomalies (Fig. 4i–l) shows a large extent of significant negative (positive) values in HFlux-driven MHWs (MCSs), while in ADV-driven events, they exhibit small horizontal extent (see supplementary discussion 3 for discrepancy between the deeper expression of SST extremes and no significant changes in MLD). This supports the idea that changes in MLD are related to changes in wind stresses and latent heat fluxes during extreme SST events when air-sea fluxes can directly influence how the upper layer is mixed[36]. It should be noted that the SST anomaly observed during an air-sea flux-driven extreme event may be influenced directly by heat flux or through a more intricate pathway: heat fluxes leading to changes in MLD, which subsequently impact SST. While we have not extensively delved into the specifics of these two processes, we can at least draw the conclusion that alterations in air-sea fluxes drive changes in MLD or SST during these extreme events, either directly or indirectly.

In both HFlux and ADV-driven MHWs/MCSs, the composite of EKE anomalies (Fig. 4m–p) does not show significant values over the BCO. This is due to the occurrence of different types of anomalous flow fields during extreme SST events. Sometimes, individual events have opposite velocity fields but the same effect over the area-averaged SST anomalies within the BCO, leading to the cancellation of EKE anomaly map and rendering the composite insignificant. We will provide a detailed analysis of this phenomenon in the next section.

Different types of flow patterns during MHWs/MCSs

The relationship between EKE and SST extreme events has been shown to be closely linked (Fig.1). However, during the onset phases of MHWs/MCSs, prominent changes in SST occur over the BCO but no significant changes were observed in the composite of EKE anomalies on most of grid points within the BCO (Fig. 4m, n, o and p). To understand this discrepancy, we examined the anomalous flow and EKE patterns during the start date (see methods) of extreme SST events (Fig. 5).

During MHWs, BC on January 4, 1993 (Fig. 5a), shows a poleward shift, leading to an increase in the horizontal heat fluxes toward the BCO (as BC is warm compared to surrounding waters). EKE anomalies (seasonal cycle removed) show negative values along the southern tip of the climatological BCO. The BC on June 17, 2010 (Fig. 5b), is strengthened, which shows positive EKE anomalies along the southern tip of the climatological BCO. Thus, the EKE anomalies cancel each other out between the two cases,

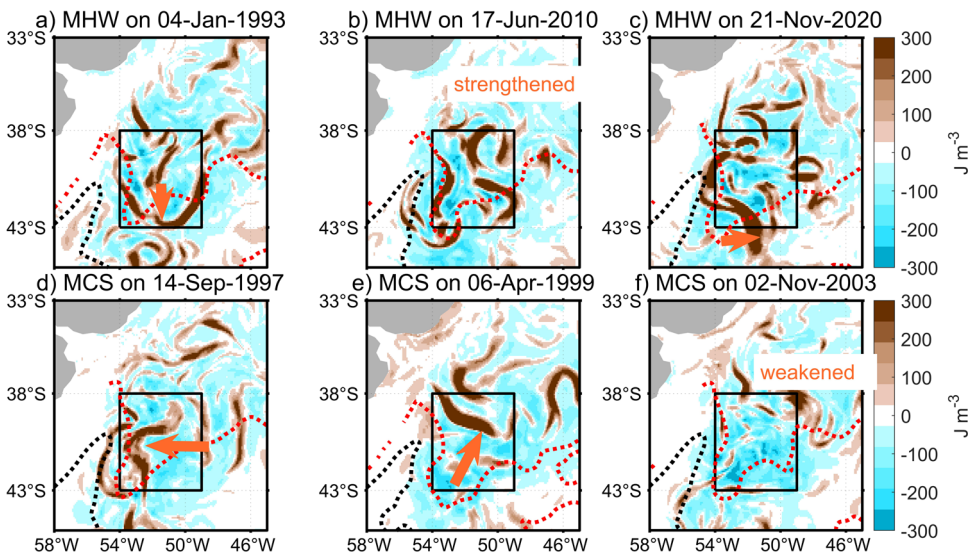

Fig. 5 | Examples of different spatial patterns of EKE anomalies during the start time of extreme SST events. The background shadings denote the composite of EKE anomalies, and the climatological daily mean position of the subtropical front (orange broken line) and the subantarctic front (black broken line). The subtropical front and subantarctic front are used here to delineate the mean positions of the BC and MC, respectively[34]. EKE anomalies during MHW events on (**a**) January 4, 1993, (**b**) June 17, 2010, and (**c**) November 21, 2020. EKE anomalies during MCS events on (**d**) September 14, 1997, (**e**) April 6, 1999, and (**f**) November 2, 2003. Anomalies are calculated by removing the seasonal cycle of daily mean values. The climatological daily mean is derived from the daily mean value averaged over 1993-2020. The orange arrows denote the shift in the position of BC. The black boxes denote the BCO regions.

and similar cases may occur over other MHW events, leading to no significant changes in the composite of EKE anomalies during the MHWs (Fig. 4n). Previous analysis has indicated that the warming observed in the western boundary extensions is primarily attributed to either the poleward shift[10,37] or intensification[9] of the west boundary currents. However, it should be noted that lateral shifts in the boundary current (east-westward) also play a role in the occurrence of MHWs (Fig. 5c).

Similar cases occur during MCSs. On September 14, 1997 (Fig. 5d), EKE is weakened in the eastern side of the BCO due to a westward shift in BC. On April 6, 1999 (Fig. 5e), the BC shrinks toward the equator, resulting in positive EKE anomalies lying on the northern sides of the BCO. This shrinkage is probably attributed to the northward shift of the BMC, as similar cases derived from the hydrographic data collected by the Spanish R/V Sarmiento de Gamboa cruise conducted between April 9 and May 10, 2016[5]. On November 2, 2003 (Fig. 5f), BC is weakened over the BCO, leading to negative anomalies over most of the BCO. Thus, the northern BCO between the two cases has opposite EKE anomalies.

The above cases explain that changes in the strength and position of the BC can cause extreme SST anomalies but no significant imprint on the composite of EKE anomalies. The processes driving the shift in BC could be due to multiple processes. For instance, the meridional shift in the BMC has been associated with the position of the zonal wind stress zero isolines[10,34] or the poleward migration of the westerlies[38]. Changes in the BC's position relative to the BMC are also linked to Rossby waves[39] or variations in gyre circulation strength, which themselves may arise due to alterations in wind stress curl[40] or coastal trapped waves[41]. Additionally, interactions between eddies and currents could exert lateral (east-westward) forces on the western boundary current[42]. The dynamics process in controlling the position of the BC could be linked to climate variability such as the Southern Annular Mode (SAM), Atlantic Niño, Pacific El Niño, and Indian Ocean Dipole (IOD)[10,38,39]. However, it is important to note that these relationships are established based on low-frequency spectral analysis or long-term linear trends. As for extreme events, the dominant climate driver impacting the BCO has yet to be definitively established. An in-depth examination of the specific causes behind the BC shift and associated climate variability during each MHW event is beyond the scope of this study.

Discussion

The Brazil Current Overshoot (BCO) is an eddy-rich region[43] and is a global warming hotspot[10]. Our findings reveal that ocean flows and air-sea heat fluxes are the two primary drivers of MHWs/MCSs (accounting for 37%/35% and 25%/33% of total events, respectively) over the BCO. These two drivers are associated with distinct patterns in the air and sea states during SST extremes. When SST extremes are driven by air-sea heat fluxes, consistent changes are observed in SST and related atmospheric variables (including both high- and low-level variations) over a wide horizontal area. Conversely, when SST extremes are driven by ocean flows, little consistency is observed in air variables and limited spatial extent of consistency among the sea variables across the majority of SST extreme events.

Using high-resolution daily reanalysis data, this study reveals that MHWs occur during high EKE and that MCSs occur during relatively low EKE. Previous studies have shown that enhanced eddy generation in western boundary current extensions leads to ocean warming[3,10]. The results of this study supplement this theory, demonstrating the connection between extremely cold sea surfaces and low EKE on a temporal perspective. In this study, the definition of EKE encompasses not only coherent mesoscale eddies but also mesoscale currents.

Previous reports have found that mesoscale flows play a vital role in determining MHW properties[44] and SST anomalies[26]. Specifically, mesoscale eddies have been identified as key drivers in the growth and dissipation of MHWs across various regions of western boundary extensions[45]. Through our statistical analysis (see supplementary discussion 1) and budget analysis (Fig. 2), we determined that coherent mesoscale eddies and mesoscale flows make a moderate contribution to observed SST extremes in the BCO. Thus, other factors must also be considered in understanding the causes of SST extremes. For example, in the case of MCSs, both mean flows and mesoscale flows are equally crucial for heat advection (Fig. 2e).

During the onset phase of sea surface heat flux-driven SST extreme events, atmospheric variables such as SLP, latent heat flux, wind stress, and 200 hPa geopotential height display significant values over an extended area. In contrast, the composites of those variables display no consistent changes in advection (ADV)-driven events. It should be noted that prominent atmospheric variable anomalies may occur outside of the BCO. For example, the maximum SLP anomalies were found on the southwestern side of the BCO (Fig. 3). The spatial distribution of SLP in HFlux-driven MHWs/MCSs is likely associated with a global atmospheric wavenumber-4 event, which propagates eastward[33].

Composite analysis of MLD, which measures the depth range of surface fluxes that have been mixed in the ocean[46], indicates consistent changes within most of SST extremes in HFlux-driven events but no significant value in ADV-driven events (Fig. 4). This suggests that air-sea fluxes, such as momentum fluxes by wind stirring and heat fluxes[36] play a dominant role in MLD variations during most extreme SST events.

During the onset phases of MHWs and MSCs, the composites of oceanic variables, including SSH, upper 0–900 m OHC, and EKE, exhibit insignificant values over the majority of the BMC. However, within the BCO region, there are a few grid points that display consistent changes in the 0–900 m OHC during advection-driven scenarios. This suggests that the SST extremes have a subsurface manifestation, which is consistent with findings reported by Elzahaby et al.[18]. It is proposed that this subsurface expression might be attributed to anomalous sea surface convergence and Ekman downwelling[47]. However, these mechanisms do not explain why, in most grid points, the composite analysis reveals insignificant EKE anomalies for both heat flux-driven and advection-driven events. Further analysis demonstrates that the flow fields exhibit diverse spatial patterns (Fig. 5), including decreases or increases in the Brazil Current (BC), meridional shifts of the BC, or zonal shifts of the BC within the BCO. These BC patterns can lead to different spatial patterns of EKE anomalies, resulting in the cancellation of EKE anomalies during the composite analysis. Previous studies have indicated that the meridional shift of the western boundary extension is influenced by the upstream stability of the western boundary[10]. Additionally, it has been suggested that the position of the BC extension can be affected by Rossby waves excited by multiple climate modes[39]. Further investigation into the specific causes of flow patterns in individual SST extreme events is necessary to fully understand the mechanisms governing these changes.

Methods

Ocean reanalysis and air-sea flux reanalysis data

To characterize extreme SST events and to calculate temperature budget terms, daily mean ocean temperatures, ocean velocities, and salinities from the Global Ocean Reanalysis and Simulations 12v1 (GLORYS 12v1[48]) data are used. This reanalysis configuration is based on the Nucleus for European Modeling of the Ocean (NEMO) ocean model, which is forced at the surface by the European Center for Medium-Range Weather Forecasts (ECMWF) ERA-Interim atmospheric reanalysis. It is distributed by the Copernicus Marine Environmental Monitoring Service (CMEMS). The horizontal resolution is 1/12° and it has 50 vertical levels, with spacing increasing with depth. The GLORYS12V1 data cover 1993 to 2020. The dynamic and thermodynamic variables from GLORYS12V1 have been compared to in situ measurements, indicating that they correctly present circulation and front patterns over the BCO[34,49,50]. This is justified by using GLORYS12V1 to study the SST extremes, but we also acknowledge that our results are sensitive to potential model biases and errors during periods and regions with limited historical observations.

Air-sea fluxes, used to calculate the net heat fluxes and derive composite maps (SLP, could cover, wind stress and geopotential height at 200 hpa), are derived from the fifth-generation ECMWF reanalysis (ERA5[51]). ERA5 employs four-dimensional variational data assimilation of in situ and satellite observations. It is constructed from the ECMWF Integrated

Forecast System. The spatial resolution is 0.25°, and the temporal resolution is hourly. We converted it to daily data to calculate heat flux terms. The ERA5 covers from 1940 to the present, and data from 1993 to 2020 are used in this study. ERA5 has been accompanied by GLORYS12V1 to identify the drivers of MHWs in previous studies[52,53] and to identify the air-sea interaction during SST extreme events.

Definition of marine heatwaves and cold spells

The definition of MHWs is adapted from Hobday et al.[13], in which the daily SST anomaly relative to a 31-day window climatology is above a seasonally varying 90th percentile threshold for each calendar day for a minimum of five consecutive days. Cold spells are defined similarly to MHWs, but SST anomalies are below their 10th percentile. SST anomalies are calculated relative to a 1993-2020 climatological period. The maximum intensity of an individual MHW/MCS event is derived from the maximum and minimum temperature anomalies observed during a heatwave/cold spell event, respectively. The maximum intensity of MHWs/MCSs for the 1993-2020 period is the maximum/minimum SST anomalies from all extreme SST events.

The start time of the SST extremes is defined following the methodology proposed by Hobday et al.[13]. Specifically, the start time is identified as the first day when the SST exceeds or falls below the 90th or 10th percentile (see Supplementary Fig. 3), respectively. The onset phase is defined as the period between the start of an extreme event (start date/onset date) and when it reaches its peak. Composites of air and sea variables are averaged over the onset phase (Figs. 3 and 4).

Eddy kinetic energy

We estimate the kinetic energy on each grid point for the mean (MKE) and eddy (EKE) fields. The time-mean flow is defined as $\bar{u}$ and $\bar{v}$, with overbars denoting time averages over the entire record. Maps of the EKE can be calculated as

$$\mathrm{EKE} = \frac{\rho_0}{2}(u'^2 + v'^2) \tag{1}$$

where the time-varying components are defined as $u'(t) = u - \bar{u}(t)$ and $v'(t) = v - \bar{v}(t)$. The density of seawater is assumed to be constant $\rho_0 = 1025\mathrm{kg\,m^{-3}}$.The units of MKE and EKE are $\mathrm{J\,m^{-3}}$.

The "eddy kinematic energy" used in this study includes not only coherent eddies but also mesoscale currents, instability waves, and other processes. This is widely accepted because many studies treat eddy-scale dynamics and anomalous velocities interchangeably[10,45,54].

Budget analysis

Mixed-layer heat budget analyses were performed to explore the relative contributions of different local drivers to MHW or MCS events over the BCO region. The budget equation[53] is written as follows:

$$\underbrace{\frac{\partial T_a}{\partial t}}_{Tend} = -\underbrace{\left[u_a\frac{\partial T_a}{\partial x} + v_a\frac{\partial T_a}{\partial y}\right]}_{ADV} - \underbrace{\left[\frac{T_a - T_{-h}}{h}\left[\frac{\partial h}{\partial t} + u_{-h}\frac{\partial h}{\partial x} + v_{-h}\frac{\partial h}{\partial y} + w_{-h}\right]\right]}_{ENT} + \underbrace{\frac{Q_{net} - Q_{pen}}{h\rho_0 c_p}}_{HFlux} + \underbrace{Residual}_{Resi} \tag{2}$$

where the subscript a denotes the variable vertically averaged between the sea surface and the bottom of the mixed layer, and the subscript $-h$ denotes the quantity at the bottom of the mixed layer. T is the temperature, T_a is the mixed layer temperature and h is the mixed layer depth (MLD), which is defined based on a 0.03 $\mathrm{kgm^{-3}}$ density threshold[55]. u and v are the horizontal velocities. w is the vertical velocity derived from the equation of volume continuity ($w_z = -\int_0^z \nabla_h \boldsymbol{u}_z dz$, $\boldsymbol{u}_z$ is the horizontal velocity at ocean level z). ρ_0 denotes the reference density (1025 $\mathrm{kg\,m^{-3}}$) and c_p denotes the heat capacity of seawater (3850 $\mathrm{J\,kg^{-1}\,°C^{-1}}$). Q_{net} is the net heat flux, and Q_{pen} is the shortwave radiation penetrating through the bottom of the MLD. Q_{pen} are derived from the same procedures as Huang et al.[56]. Q_{net} is the sum of net contributions from shortwave radiation (Q_{SW}), longwave radiation (Q_{LW}), sensible heat fluxes (Q_{Sen}) and the latent heat fluxes (Q_{Lat}). Positive heat fluxes denote the sea surface receiving heat.

$$Q_{net} = Q_{SW} + Q_{LW} + Q_{Sen} + Q_{Lat} \tag{3}$$

The left-hand side of Eq. (2) denotes the temperature tendency (Tend). The first right-hand side term (in parentheses) in Eq. (2) denotes horizontal advection (ADV), the second right-hand side term denotes entrainment (ENT), and the third right-hand side terms denote heat fluxes (HFlux). The fourth term denotes the residual, which is the difference between Tend and the sum of ADV, ENT, and HFlux. The residual term is composed of various factors, encompassing horizontal and vertical diffusion, calculation errors, as well as other terms that have not been considered in the budget equation.

To identify the dominant driver of MHWs/MCSs at each grid point in each event, we calculate the anomalies of the right-hand side terms of Eq. (2) relative to the daily climatological mean value and integrate the anomalies in time (from the start time of the SST extreme events to the peak time of SST extremes). It is evident that the SST anomalies have already accumulated to a noticeable extent before the defined start time. Thus, we have defined the initial time of heat integration as the local minimum point just prior to the initiation of MHWs, and vice versa for MCSs (Supplementary Fig. 3). Then, the cumulative values are compared, and we classify them as HFlux-driven SST extremes if the net heat flux is the dominant force, ADV-driven SST extremes if horizontal advection plays the most important role, ENT-driven SST extremes if vertical entrainment is the dominant term, Resi-driven SST extremes if the unresolved term is the dominant term and "mixed-driven" SST extremes if the difference between the first dominant and the second dominant term is 10% or less[18].

To further investigate the relative contribution of mean flow and mesoscale flow in horizontal advection, ADV anomalies can be divided based on approaches from Bian et al.[45]:

$$\begin{aligned}&\left(u\frac{\partial T}{\partial x} + v\frac{\partial T}{\partial y}\right)',\\ &= \underbrace{\left(\bar{u}\frac{\partial \bar{T}}{\partial x} + \bar{v}\frac{\partial \bar{T}}{\partial y}\right)}_{HFC-M} + \underbrace{\left[\left(u'\frac{\partial T'}{\partial x} + v'\frac{\partial T'}{\partial y}\right) + \left(\bar{u}\frac{\partial T'}{\partial x} + \bar{v}\frac{\partial T'}{\partial y}\right) + \left(u'\frac{\partial \bar{T}}{\partial x} + v'\frac{\partial \bar{T}}{\partial y}\right)\right]}_{HFC-E}\end{aligned} \tag{4}$$

The mean flow signals, represented by an overbar, are determined through a 3° × 3° spatial running mean. On the other hand, the mesoscale eddy (flow) fields, indicated by a prime, are calculated as deviations from this 3° × 3° spatial mean. The terms within the first bracket on the right-hand side signify the advection caused by the mean flow (HFC-M), while the second term represents the advection driven by the mesoscale eddies (HFC-E, i.e., mesoscale flows). The definition of HFC-E follows the methodology outlined in Bian et al.[45]. However, it is important to note that the procedure used does not allow us to distinguish coherent mesoscale eddies from other mesoscale flows. Therefore, in this study, we refer to HFC-E as mesoscale flows rather than specifically identifying them as coherent mesoscale eddies.

Data availability

All data used in this study are available online. GLORYS reanalysis data are freely available at: https://resources.marine.copernicus.eu/products. ERA5 hourly data were obtained from https://cds.climate.copernicus.eu/cdsapp#!/dataset/reanalysis-era5-single-levels?tab=form.

Code availability

All analyses were performed using MATLAB. The source code used to make the calculations and plots in this paper are available from the corresponding

author on request or scripts used for producing the figures will be available on Github at publication (https://github.com/lortty163/SST-extremes-on-BCO).

Received: 31 May 2023; Accepted: 6 February 2024;
Published online: 26 February 2024

References

1. Saraceno, M., Provost, C., Piola, A. R., Bava, J. & Gagliardini, A. Brazil Malvinas Frontal System as seen from 9 years of advanced very high resolution radiometer data. *J. Geophys. Res.: Oceans* **109** (2004).
2. Francisco, C. P. F., Silveira, I. C. Ada & Campos, E. J. D. Dynamics of the Brazil-Malvinas confluence: energy conversions. *J. Phys.: Conf. Ser.* **285**, 012045 (2011).
3. Martínez-Moreno, J. et al. Global changes in oceanic mesoscale currents over the satellite altimetry record. *Nat. Clim. Change* **11**, 397–403 (2021).
4. Jullion, L., Heywood, K. J., Garabato, A. C. N. & Stevens, D. P. Circulation and water mass modification in the Brazil–Malvinas confluence. *J. Phys. Oceanogr.* **40**, 845–864 (2010).
5. Manta, G. et al. Shelf water export at the brazil-malvinas confluence evidenced from combined in situ and satellite observations. *Front. Mar. Sci.* **9** (2022).
6. Barton, A. D., Dutkiewicz, S., Flierl, G., Bragg, J. & Follows, M. J. Patterns of diversity in marine phytoplankton. *Science* **327**, 1509–1511 (2010).
7. Clayton, S., Dutkiewicz, S., Jahn, O. & Follows, M. J. Dispersal, eddies, and the diversity of marine phytoplankton. *Limnol. Oceanogr.: Fluids. Environ.* **3**, 182–197 (2013).
8. de Moura Falcão, R. H., de Castro Melo, P. A. M., de Araujo Filho, M. C. & da Glória Gonçalves da Silva Cunha, M. Brazil-Malvinas Confluence in the South-West Atlantic Ocean: phytoplankton species, life forms and trophic mode. *Botanica Marina* **65**, 391–403 (2022).
9. Wu, L. et al. Enhanced warming over the global subtropical western boundary currents. *Nat. Clim. Change* **2**, 161–166 (2012).
10. Li, J., Roughan, M. & Kerry, C. Drivers of ocean warming in the western boundary currents of the Southern Hemisphere. *Nat. Clim. Change* **12**, 901–909 (2022).
11. Leyba, I. M., Saraceno, M. & Solman, S. A. Air-sea heat fluxes associated to mesoscale eddies in the Southwestern Atlantic Ocean and their dependence on different regional conditions. *Clim. Dyn.* **49**, 2491–2501 (2017).
12. Perez, J. A. A. & Sant'Ana, R. Tropicalization of demersal megafauna in the western South Atlantic since 2013. *Commun. Earth Environ.* **3**, (2022).
13. Hobday, A. J. et al. A hierarchical approach to defining marine heatwaves. *Prog. Oceanogr.* **141**, 227–238 (2016).
14. Manta, G., Mello, S., de, Trinchin, R., Badagian, J. & Barreiro, M. The 2017 record marine heatwave in the Southwestern Atlantic Shelf. *Geophys. Res. Lett.* **45,**12,449 - 12,456 (2018).
15. Rodrigues, R. R., Taschetto, A. S., Gupta, A. S. & Foltz, G. R. Common cause for severe droughts in South America and marine heatwaves in the South Atlantic. *Nat. Geosci.* **12**, 620–626 (2019).
16. Schlegel, R. W., Darmaraki, S., Benthuysen, J. A., Filbee-Dexter, K. & Oliver, E. C. J. Marine cold-spells. *Prog. Oceanogr.* **198**, 102684 (2021).
17. Gregory, C. H., Holbrook, N. J., Marshall, A. G. & Spillman, C. M. Atmospheric drivers of Tasman Sea marine heatwaves. *J. Clim.* **36**, 5197–5214 (2023).
18. Elzahaby, Y., Schaeffer, A., Roughan, M. & Delaux, S. Oceanic circulation drives the deepest and longest marine heatwaves in the East Australian current system. *Geophys. Res. Lett.* **48**, e2021GL094785 (2021).
19. Hayashida, H., Matear, R. J., Strutton, P. G. & Zhang, X. Insights into projected changes in marine heatwaves from a high-resolution ocean circulation model. *Nat. Commun.* **11**, 4352 (2020).
20. Jacox, M. G. et al. Global seasonal forecasts of marine heatwaves. *Nature* **604**, 486–490 (2022).
21. Holbrook, N. J. et al. A global assessment of marine heatwaves and their drivers. *Nat. Commun.* **10** (2019).
22. Marin, M., Feng, M., Bindoff, N. L. & Phillips, H. E. Local drivers of extreme upper ocean marine heatwaves assessed using a global ocean circulation model. *Front. Clim.* **4** (2022).
23. Vogt, L., Burger, F. A., Griffies, S. M. & Frölicher, T. L. Local drivers of marine heatwaves: a global analysis with an earth system model. *Front. Clim.* **4** (2022).
24. Frenger, I., Münnich, M., Gruber, N. & Knutti, R. Southern Ocean eddy phenomenology. *J. Geophys. Res.: Oceans* **120**, 7413–7449 (2015).
25. Chelton, D. B., Schlax, M. G., Samelson, R. M. & Szoeke, R. A. de. Global observations of large oceanic eddies. *Geophys. Res. Lett.* **34** (2007).
26. Cabrera, M. et al. The southwestern Atlantic Ocean mesoscale eddies: a review of their role in the air-sea interaction processes. *J. Mar. Syst.* **235**, 103785 (2022).
27. Magalhães, F. C., Azevedo, J. L. L. & Oliveira, L. R. Energetics of eddy-mean flow interactions in the Brazil current between 20°S and 36°S. *J. Geophys. Res.: Oceans* **122**, 6129–6146 (2017).
28. Frölicher, T. L. & Laufkötter, C. Emerging risks from marine heat waves. *Nat. Commun.* **9**, 650 (2018).
29. Hausmann, U. & Czaja, A. The observed signature of mesoscale eddies in sea surface temperature and the associated heat transport. *Deep Sea Res. Part I: Oceanogr. Res. Papers* **70**, 60–72 (2012).
30. Gaube, P., Chelton, D. B., Samelson, R. M., Schlax, M. G. & O'Neill, L. W. Satellite observations of mesoscale Eddy-induced Ekman pumping. *J. Phys. Oceanogr.* **45**, 104–132 (2015).
31. Perkins-Kirkpatrick, S. E. et al. The role of natural variability and anthropogenic climate change in the 2017/18 Tasman sea marine heatwave. *Bull. Am. Meteorol. Soc.* **100**, S105–S110 (2019).
32. Rodrigues, R. R. & Woollings, T. Impact of atmospheric blocking on South America in austral summer. *J. Clim.* **30**, 1821–1837 (2017).
33. Chiswell, S. M. Atmospheric wavenumber-4 driven South Pacific marine heat waves and marine cool spells. *Nat. Commun.* **12**, 4779, (2021).
34. Artana, C. et al. The Malvinas current at the confluence with the Brazil Current: inferences from 25 years of Mercator Ocean reanalysis. *J. Geophys. Res.: Oceans* **124**, 7178–7200 (2019).
35. Pezzi, L. P. et al. Oceanic eddy-induced modifications to air–sea heat and CO2 fluxes in the Brazil-Malvinas confluence. *Sci. Rep.* **11**, 10648 (2021).
36. Liu, H., Lin, X. & Lan, J. Salt sinking in the upper South Pacific Subtropical Gyre from 2004 to 2016. *J. Geophys. Res.: Oceans* **124**, 7011–7029 (2019).
37. Oliver, E. C. J. et al. The unprecedented 2015/16 Tasman Sea marine heatwave. *Nat. Commun.* **8**, 16101 (2017).
38. Qu, T., Fukumori, I. & Fine, R. A. Spin-Up of the Southern Hemisphere Super Gyre. *J. Geophys. Res.: Oceans* **124**, 154–170 (2019).
39. Bodnariuk, N., Simionato, C. G., Osman, M. & Saraceno, M. The Río de la Plata plume dynamics over the Southwestern Atlantic Continental Shelf and its link with the large scale atmospheric variability on interannual timescales. *Continental Shelf Res.* **212**, 104296 (2021).
40. Marcello, F., Wainer, I. & Rodrigues, R. R. South Atlantic Subtropical Gyre late twentieth century changes. *J. Geophys. Res.: Oceans* **123**, 5194–5209 (2018).
41. Poli, L., Artana, C. & Provost, C. Topographically trapped waves Around South America with periods between 40 and 130 Days in a global ocean reanalysis. *J. Geophys. Res.: Oceans* **127**, e2021JC018067 (2022).
42. Li, J., Roughan, M. & Hemming, M. Interactions between cold cyclonic eddies and a western boundary current modulate marine heatwaves. *Commun. Earth. Environ.* **4** (2023).
43. Chelton, D. B., Schlax, M. G. & Samelson, R. M. Global observations of nonlinear mesoscale eddies. *Prog. Oceanogr.* **91**, 167–216 (2011).

44. Pilo, G. S., Holbrook, N. J., Kiss, A. E. & Hogg, A. McC. Sensitivity of marine heatwave metrics to ocean model resolution. *Geophys. Res. Lett.* **46**, 14604–14612 (2019).
45. Bian, C. et al. Oceanic mesoscale eddies as crucial drivers of global marine heatwaves. *Nat. Commun.* **14**, 2970 (2023).
46. Brainerd, K. E. & Gregg, M. C. Surface mixed and mixing layer depths. *Deep Sea Res. Part I: Oceanogr. Res. Papers* **42**, 1521–1543 (1995).
47. Hu, S. et al. Observed strong subsurface marine heatwaves in the tropical western Pacific Ocean. *Environ. Res. Lett.* **16**, 104024 (2021).
48. Jean-Michel, L. et al. The Copernicus Global 1/12° oceanic and sea ice GLORYS12 reanalysis. *Front. Earth Sci.* **9** (2021).
49. Artana, C., Lellouche, J., Sennéchael, N. & Provost, C. The open-ocean side of the Malvinas current in Argo floats and 24 Years of Mercator Ocean high-resolution (1/12) physical reanalysis. *J. Geophys. Res.: Oceans* **123**, 8489–8507 (2018).
50. Orúe-Echevarría, D. et al. A view of the Brazil-Malvinas confluence, March 2015. *Deep Sea Res. Part I: Oceanogr. Res. Papers* **172**, 103533 (2021).
51. Hersbach, H. et al. The ERA5 global reanalysis. *Q. J. Roy. Meteorol. Soc.* **146**, 1999–2049 (2020).
52. Oh, H. et al. Classification and causes of East Asian marine heatwaves during Boreal summer. *J. Clim.* **36**, 1435–1449 (2023).
53. Liu, H., Nie, X., Cui, C. & Wei, Z. Compound marine heatwaves and low sea surface salinity extremes over the tropical Pacific Ocean. *Environ. Res. Lett.* **18**, 064001 (2023).
54. Zhou, G. & Cheng, X. On the errors of estimating oceanic eddy kinetic energy. *J. Geophys. Res.: Oceans* **126**, e2020JC016449, (2021).
55. de Boyer Montégut, C., Madec, G., Fischer, A. S., Lazar, A. & Iudicone, D. Mixed layer depth over the global ocean: an examination of profile data and a profile-based climatology. *J. Geophys. Res.: Oceans* **109** (2004).
56. Huang, B., Xue, Y., Zhang, D., Kumar, A. & McPhaden, M. J. The NCEP GODAS ocean analysis of the tropical pacific mixed layer heat budget on seasonal to interannual time scales. *J. Clim.* **23**, 4901–4925 (2010).

Acknowledgements

This study was supported jointly by the National Natural Science Foundation of China (Grant 42006005), the Laoshan Laboratory (No. LSKJ202202700), and Qilu University of Technology: The Basic Research Category Projects of the Pilot Integration of Science, Education, and Industry (2023PY044).

Author contributions

H.L., X.W.N. and Z.X.W. initiated the research. H.L. conducted the analysis and drafted the MS with input from X.W.N. and Z.X.W. J.Q.S. helped with processing codes.

Competing interests

The authors declare no competing interests.

Additional information

Supplementary information The online version contains supplementary material available at https://doi.org/10.1038/s43247-024-01258-1.

Correspondence and requests for materials should be addressed to Hao Liu or Zexun Wei.

Peer review information *Communications Earth & Environment* thanks the anonymous reviewers for their contribution to the peer review of this work. Primary Handling Editors: Jennifer Veitch, Clare Davis, Heike Langenberg. A peer review file is available.